Carbon Trends 12 (2023) 100283

Contents lists available at ScienceDirect

Carbon Trends

journal homepage: www.elsevier.com/locate/cartre

Carbon film produced from microwave-driven methane pyrolysis

Mehran Dadsetan[a], Kenneth G. Latham[b], Boran Kumral[a], Mohammad Fawaz Khan[a], Mia Scott[a], Tirthankar Mitra[a], Ali Naseri[a], Sama Manzoor[c], Erin R. Bobicki[c], Tobin Filleter[a], Maria-Magdalena Titirici[b], Murray J. Thomson[a,*]

[a] Department of Mechanical and Industrial Engineering, University of Toronto, 5 King's College Road, Toronto, ON, M5S 3G8, Canada
[b] Department of Chemical Engineering, Imperial College London, South Kensington Campus, London SW7 2AZ, United Kingdom
[c] Department of Chemical and Materials Engineering, University of Alberta, 116St & 85 Ave, Edmonton, Alberta, T6G 2R3, Canada

ARTICLE INFO

Keywords:
Conductive carbon film
Thin film carbon
Methane pyrolysis
Microwave-driven pyrolysis

ABSTRACT

Methane pyrolysis is a widely used technique for producing hydrogen and valuable carbon materials. Among these materials are carbon films, which have a diverse range of properties that make them useful for various applications. This study focuses on synthesizing a new type of carbon film through a microwave-driven methane pyrolysis process. The resulting metallic-like carbon film deposits on a polished quartz substrate and detaches as it thickens. We conducted a thorough characterization of the film's properties, using different techniques to study its surface morphology and structural features. Our findings show that the carbon film has a smooth surface texture and a semi-graphitic internal structure, with 78% of the carbon atoms exhibiting sp2 bonding as revealed by X-ray photoelectron spectroscopy. X-ray diffraction analysis further confirms the presence of microcrystalline carbon fragments within the film. Additionally, conductivity measurements using a conductive-atomic force microscope demonstrate the carbon film's remarkable electrical conductivity, comparable to that of gold and silver metals. The electrochemical measurements indicate that the carbon film's high conductivity and free-standing nature make it a promising candidate for use as a direct active material in sodium-ion batteries. This is because the film does not require binders or conductive agents, which can improve battery performance.

1. Introduction

Methane pyrolysis is a widely used method for producing hydrogen and valuable carbon materials [1]. The types of carbon materials generated through pyrolysis depend on several factors, including temperature, pressure, gas composition, utilization of catalysts, and pre- or post-pyrolysis processing steps [2–4]. These parameters can affect the kinetics, end structures, and texture of the final product, resulting in a diverse range of carbon materials, such as carbon nanotubes (CNTs) [5], carbon black [6], graphene [7], and pyrolytic bulk carbon [8].

Thin film carbon formation has been studied for several decades. Carbon films exhibit a wide range of properties, making them useful for various applications. The mechanical, electrochemical, and electrical properties of a carbon film depend on the method of production. Diamond-like carbon (DLC) films, one of the most widely used types of carbon films, were first produced by Aisenberg and Chabot [9] using ion-beam deposition. Structural analysis of various DLC films reveals that they consist of a mixture of sp2 and sp3 bonded carbon atoms, with the proportion of sp3 content ranging from 33% to 60% depending on the experimental conditions [10]. It has been reported that DLC possesses desirable mechanical and electrochemical properties [11], which can be adjusted by modifying the experimental conditions and precursor material [12]. Methane pyrolysis has been found an effective method for the growth of diamond-like carbon films in a controlled environment [13].

Graphene exists in various forms, notably in the form of small sheets and large-area films [14] which is mainly produced through liquid-phase exfoliation of graphite [15]. However, the exfoliation process can be complex and present environmental concerns [16]. As an alternative, methane pyrolysis has been explored as a method to produce high-purity graphene for use as a conductive agent in lithium-ion batteries [17]. Additionally, graphene oxide [18] can be obtained through further processing of the hydrogenated amorphous carbon resulting from methane pyrolysis [19]. Graphene oxide possesses unique properties attributable to the presence of oxygen functional groups, making it suitable for various applications in electronics [20].

The microwave-plasma method has been employed for the production of various types of carbon films, including amorphous structures as well as graphitic carbon sheets. This process involves the decomposition of hydrocarbons and alcohols within a high-temperature environment [21–23]. It has been reported that the addition of hydrogen affects

* Corresponding author.
E-mail address: murray.thomson@utoronto.ca (M.J. Thomson).

https://doi.org/10.1016/j.cartre.2023.100283
Received 8 May 2023; Received in revised form 18 June 2023; Accepted 6 July 2023
2667-0569/© 2023 Published by Elsevier Ltd. This is an open access article under the CC BY-NC-ND license (http://creativecommons.org/licenses/by-nc-nd/4.0/)

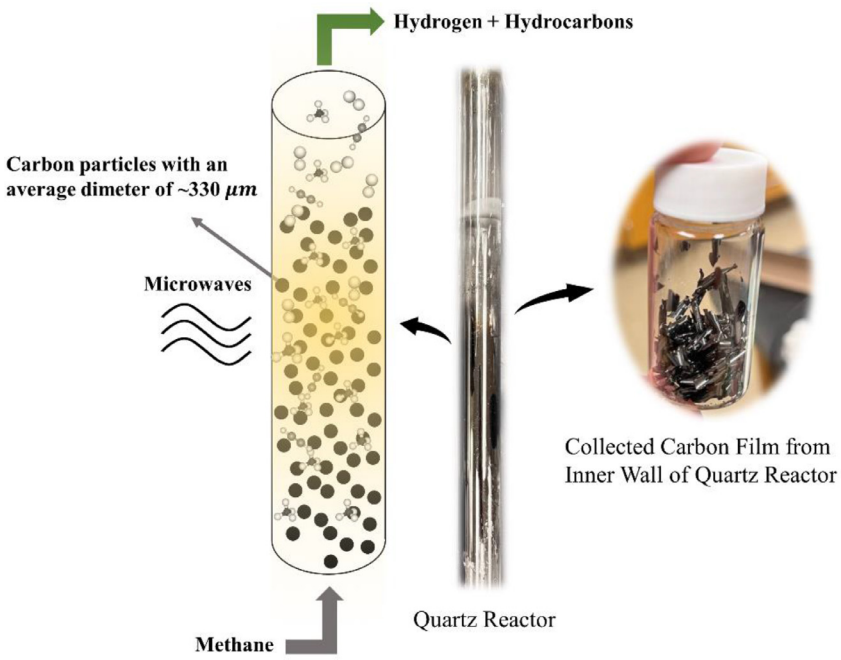


Fig. 1. Experimental Setup for Carbon Film Formation. A continuous carbon film is formed on the inner surface of the reactor's hot wall during methane pyrolysis at temperatures ~1000°C.

the ordering in the structure of the carbon sheets, promoting a more graphitic-like structure [24]. Additionally, the presence of oxygen has been found to facilitate the formation of graphene [25].

Moreover, non-thermal plasma decomposition of methane was employed to synthesize nanoflake graphene [26]. However, despite efforts to produce graphene, the final product may suffer from contamination by other carbon by-products, such as carbon nanotubes [27]. Consequently, novel methane pyrolysis methods in conjunction with microwave [28] and radiofrequency [28] have been introduced to mitigate contamination issues associated with the pyrolysis process, resulting in the production of pure graphene. Notably, the "pulse-etched" microwave-induced "snowing" technique has been employed to produce low-oxygen content graphene [29,30], and graphene nanosheets were synthesized through radio-frequency induction thermal plasma methane pyrolysis [31].

The comparison between DLC and graphene-based carbon films reveals notable differences in their properties. DLC films typically have a hardness value ranging between 15 GPa [32] to 50 GPa [33], depending on the production method [34]. On the other hand, graphene-based carbon films exhibit a lower hardness value in the range of 5±2 GPa [35] due to the greater presence of sp2 carbon-bonded atoms. Regarding electrical conductivity, DLC films consist of a significant amount of sp3 bonded carbon atoms, resulting in low electrical conductivity [36]. However, it is worth noting that the electrical conductivity of DLC films can be enhanced through certain modifications [37]. In contrast, graphene-based carbon films possess a higher sp2 content, which enhances charge transport efficiency. This is exemplified by the high conductivity of graphene at approximately ~2000 S m-1 [38]. Due to this characteristic, graphene-based carbon films find extensive application in the field of semiconductors [39].

In this study, we synthesized a new form of carbon film with a semi-graphitic structure and metallic properties on the polished quartz surface (i.e., inner wall of the reactor) using microwave-driven methane pyrolysis process. For detailed information on the experiment of methane pyrolysis using microwaves refer to [40]. Previous studies have investigated carbon films [41] indicting that at elevated temperatures and long residence times, the process of pyrolytic carbon deposition begins with the creation of polycyclic aromatic hydrocarbons (PAHs) and other hydrocarbons which aggregate as droplets, subsequently condensing onto a substrate and undergoing a transformation into pyrolytic carbon [42]. However, the characterization of these carbon films has not been thoroughly explored. Here in this study, the objective is to comprehensively characterize the carbon film produced through a novel method of methane pyrolysis using microwaves. In the following, we begin with the characterization of surface morphology and bulk structure using scanning transmission electron microscopy and focused ion beam – high-resolution transmission electron microscopy techniques, respectively. Chemical composition and structural features are revealed through X-ray photoelectron spectroscopy, X-ray diffraction, and Raman spectroscopy. Then, a detailed discussion of the potential pathways for carbon film formation has been provided. Conductive atomic force microscopy is used to measure the film's conductivity, and its performance in Na-ion batteries is evaluated through electrochemical measurements. These analyses help us gain a deeper understanding of the unique features of this type of carbon film.

2. Materials and methods

Fig. 1 shows the schematic of the experimental setup. The setup includes a 660.4mm-long (OD = 25.4 mm and ID = 22 mm) quartz reactor vertically inserted into a 1 kW microwave. The quartz reactor is designed to withstand high temperatures, with an annealing point of 1215°C and a softening point of 1683°C. The reactor was filled with carbon particles that serve as the absorbing medium for the microwave energy used to drive the methane pyrolysis reaction. The reaction breaks down methane into solid carbon and hydrogen, with minor byproducts of C1 and C2 hydrocarbons. A comprehensive discussion of the experimental procedure can be found in [40].

During methane pyrolysis, over 99% of the solid carbon produced is deposited on the surface of the particles, while less than 1% forms carbon films on the hot wall of the quartz reactor. The carbon film collected from the inner wall of the reactor, illustrated in Fig. 1, has a shiny, metallic appearance. The carbon film's thickness varies at different heights along the reactor, depending on the temperature of the hot wall at those locations. The experimental results revealed that the carbon film formed in hotter regions (i.e., near hot spots generated by the microwave field) is thicker than that formed in colder regions near the exhaust.

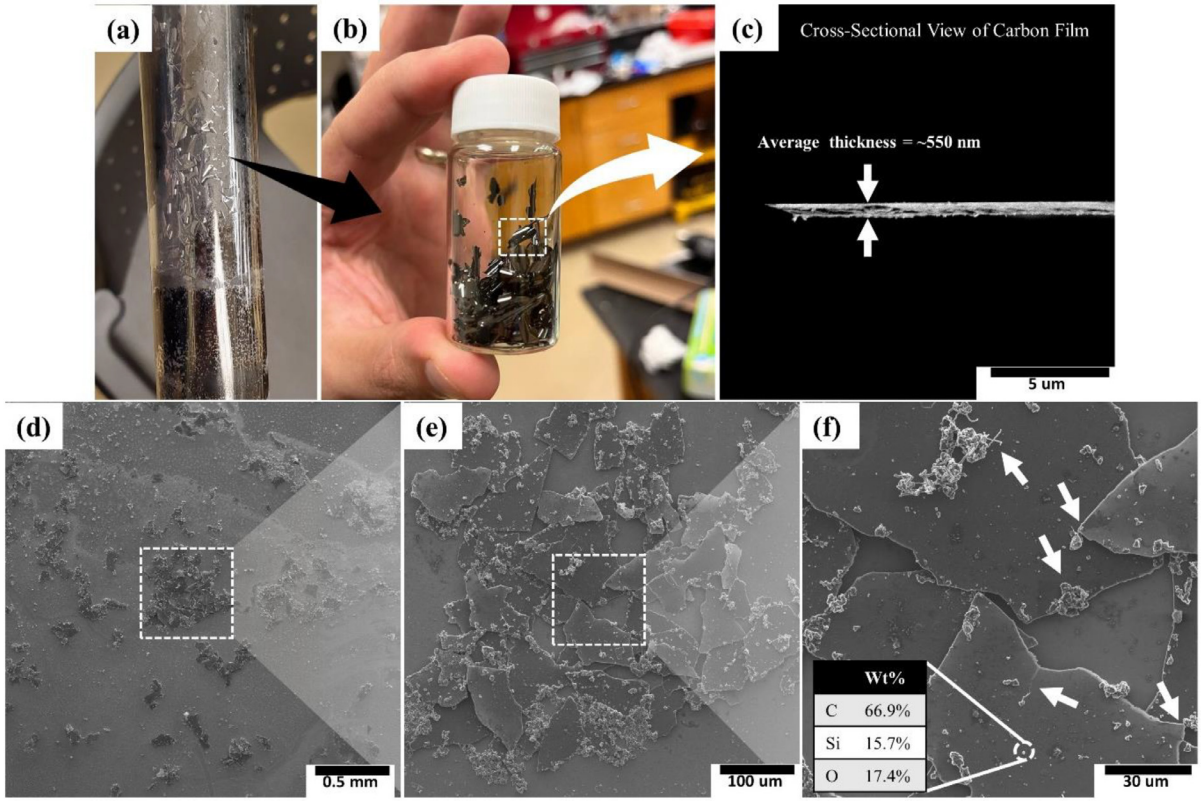


Fig. 2. SEM Images of the Carbon Film, Cross-Sectional Thickness Measurement, and Contamination Analysis. The carbon film was collected from the inner wall of the reactor and drop-coated onto a silicon wafer chip. The tilt of the carbon film allowed for cross-sectional thickness measurement. The contamination observed on the carbon film was primarily attributed to the granular carbon particles and the quartz reactor.

3. Results and discussion

3.1. Surface morphology analysis of thin carbon film

A representative sample of carbon film was selected from a region near the hot zone of the reactor. To prepare the carbon film samples for imaging, they were first dispersed in ethanol and then drop-coated onto a silicon chip substrate. The substrate was inserted into a scanning electron microscope (SEM) with bright-field and dark-field detectors (FEI Quanta FEG 250). The thickness of the sample was measured using an ultra-high-resolution Schottky scanning electron microscope (SU7000). In addition, an energy-dispersive X-ray spectroscopy (EDX) point scan was performed to identify the composition of contaminants found on the surface of the carbon film. Fig. 2 illustrates the results of all the aforementioned measurements.

During the experiment, carbon films are formed on the polished quartz reactor. As there is no chemical bonding between the quartz and carbon, the film naturally detaches as it thickens. After collecting the carbon film from the region indicated in Fig. 2a, it was stored in the container displayed in Fig. 2b and later used for SEM imaging. The SEM image depicted in Fig. 2c presents a cross-sectional view of a tilted carbon film, revealing that the film produced near the microwave's hot spots has a thickness of approximately 550 nm.

The surface morphology of the carbon film, as shown in the SEM images presented in Fig. 3d to 3f, indicates that the film has a smooth texture on its surface. Furthermore, the conducted BET surface analysis has yielded a surface area of 2.94 m2/g, suggesting a smooth surface for the carbon film. However, it is important to acknowledge that this relatively small surface area is prone to errors, primarily due to the limited amount of surface area available for measurement and the low quantity of the sample. The presence of sharp edges and the crack pointed out by the arrows in Fig. 2f suggests that the carbon film has a brittle nature. The irregular-shaped carbon objects embedded with carbon fibers, which were detected on the carbon film, mostly originated from the carbon particles that came into contact with the film during the pyrolysis process. In addition, dots with different contrast on the surface of the carbon film were analyzed using EDX point scan, which revealed that they contain around 66.9% carbon. The remaining composition mostly comprises oxygen and silicon, with less than 1% of other elements. The source of these contaminants is most likely the granular carbon particles and contact between the carbon film and the quartz reactor. However, it is also possible that they originated from materials used during sample handling or components and parts upstream of the experimental setup.

3.2. X-ray photoelectron spectroscopy (XPS) characterization of carbon film surface

The carbon film was analyzed using a ThermoFisher SCIENTIFIC K-Alpha X-ray Photoelectron Spectrometer, which is equipped with a monochromated AI K X-ray source. XPS analysis can identify the distinctive chemical and structural features of the top 10 nm of the carbon film [43]. This is achieved by studying the XPS survey spectrum and C1s chemical state of the carbon film [44], which helps in identifying the sp2 hybridized carbon atoms and the degree of graphitization of the carbon film. Analysis of the XPS spectra reveals that the carbon film is predominantly composed of 97.4% carbon, 2.5% oxygen, and less than 1% silicon. It's noteworthy that despite the absence of oxygen during the production process, the film contains less than 3% oxygen, suggesting possible exposure to air during transfer for analysis [45]. Additionally, the oxygen and silicon present in the film may be due to SiO_2 residue left behind during detachment from the reactor walls.

To gain insight into the structure of the carbon film, its XPS survey was compared with those of activated carbon and graphite flakes, which are commonly used as representatives of amorphous and graphitic car-

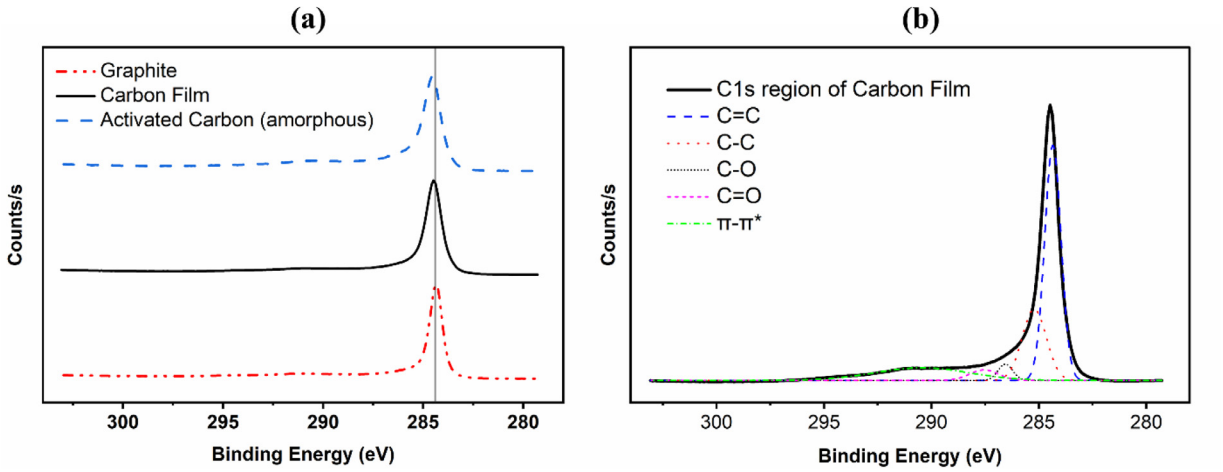


Fig. 3. XPS C1s Spectra of Carbon Film, Activated Carbon, and Graphite. The position of the main peak for the carbon film lies between the two peaks for activated carbon and graphite, suggesting its semi-graphitic structure. The deconvolution of the C1s XPS spectrum of the carbon film was used to determine its sp2 percentage.

bon, respectively. This comparison is presented in Fig. 3a. Across all spectra, the dominant peak is centered between 284.4 to 285.1, which can be attributed to carbon atoms with sp2 and sp3 hybridization. The dashed line denotes the binding energy of sp2 hybridized carbon atoms, which is 284.4 eV [10]. The peak for the carbon film is situated between the values observed for activated carbon and graphite, suggesting that the film has a semi-graphitic structure. To further examine the C1s XPS spectrum of the carbon film, the peaks corresponding to C = C (284.4 eV) [46], C–C (285.1 eV) [47], C–O (285.9 eV) [46,48], C = O (287.4 eV) [46], and π-π^* (291.3 eV) [49] bonds were deconvoluted based on their respective binding energies [44] using Origin software, which yielded an adjusted R-squared value of 0.977. The resulting deconvoluted curve for the carbon film is presented in Fig. 3b. By deconvoluting the C1s chemical state, the components representing different types of bonding between carbon-carbon and carbon-oxygen were identified. To calculate the sp2 fraction, the corresponding peak area was determined and divided by the total C1s peak area. This ratio was then further normalized using the reference value obtained for graphite flakes. The analysis reveals that the carbon film has a semi-graphitic structure, with approximately 78% of the carbon atoms exhibiting sp2 bonding.

3.3. Characteristics of carbon film through Raman spectroscopy and X-ray diffraction (XRD) analysis

Raman spectroscopy was performed using a Renishaw inVia™ Raman microscope with an incident wavelength of 532 nm from a diode-pumped solid-state laser with a 20x objective, resulting in a spot size of ~1.4 μm. To prevent local heating induced by the laser, the intensity was kept at a constant value of around 1 mW. Fig. 4a illustrates the Raman spectrum obtained from the carbon film, where the Raman curve has been deconvoluted by considering four major bands. These include T (I, D4) band around 1200 cm^{-1}, D (D1) band at 1349 cm^{-1}, G band at 1596 cm^{-1}, and A (D", D3) band at around 1520 cm^{-1} [50]. The D and G bands originate from disorder in the carbon structure [51–53], such as armchairs and zigzag edges [54], while the G band arises from the ideal graphitic lattice [51–53] in the carbon structure. The T band is also associated with the graphite lattice disordering, similar to the D band, while the A band is related to amorphous carbon features [53].

The degree of graphitization in carbon samples is commonly evaluated by analyzing the ratio of the D band intensity to the G band intensity (I_D/I_G). For the carbon film produced by microwave-driven methane pyrolysis, an I_D/I_G ratio of 1.31 has been measured. Furthermore, it has also been reported [50] that glassy carbon exhibits a distinctive characteristic of an I_D/I_G ratio exceeding 1. The characterization conducted in this study shows that the carbon film has a semi-graphitic nature, as indicated by the Raman analysis, which closely resembles this feature found in glassy carbon.

Table 1
The lateral size (La) and stacking height (Lc) of activated carbon, carbon film, and graphite flakes, which have been calculated using Eqs. (1) and 2.

Sample	L_c (nm)	L_a (nm)
Activated Carbon	1.01	4.00
Carbon Film	3.41	4.41
Graphite	26.14	–

Furthermore, Fig. 4b displays the X-ray diffraction (XRD) patterns of the carbon film, activated carbon (representing amorphous carbon), and graphite, obtained utilizing a Bruker D8 Advance diffractometer over a 2θ range of 5° to 110°, using Cu-Kα radiation with a wavelength of 1.5418 Å. Subsequently, the spectra were processed using Origin software to determine the FWHM and peak positions, which were then utilized to determine the lateral size (La) and stacking height (Lc) of the carbon samples using the Scherrer equations (Eq.1 and 2) [55,56]. The resulting values of La and Lc for all three samples can be found in Table 1.

$$L_a = \frac{1.84\lambda[=1.54178\text{nm}]/\beta_a\left[\text{FWHMof(101)peak}\right]}{\cos\left(\theta_a\left[\text{Braggangleof(101)peak}\right]\right)} \quad (1)$$

$$L_c = \frac{0.89\lambda[=1.54178\text{nm}]/\beta_c\left[\text{FWHMof(002)peak}\right]}{\cos\left(\theta_c\left[\text{Braggangleof(002)peak}\right]\right)} \quad (2)$$

The X-ray diffraction spectra show two distinct peaks: one between 24.8° to 26.4° corresponding to the (002) reflection, and the other between 43° to 43.7° corresponding to the (101) reflection. In addition, the graphite spectrum exhibits a second peak at 54.5°, corresponding to the (004) reflection. The carbon film displays a second peak at $2\theta = 30°$, which may be attributed to Si impurity as identified in XPS results [57]. The sharp (002) peak in the carbon samples, similar to graphite's peak, indicates a crystalline structure. However, the broader peak suggests the presence of random microcrystalline fragments [58], as seen in activated carbon and pyrolytic carbon film spectra. By comparing the position of the (002) peak in all three samples, it is evident that the carbon film's peak center falls between that of activated carbon and graphite. This indicates the presence of microcrystalline carbon fragments within the carbon film [58]. Additionally, comparison of the lateral width and stacking height values obtained for all three carbon samples provides

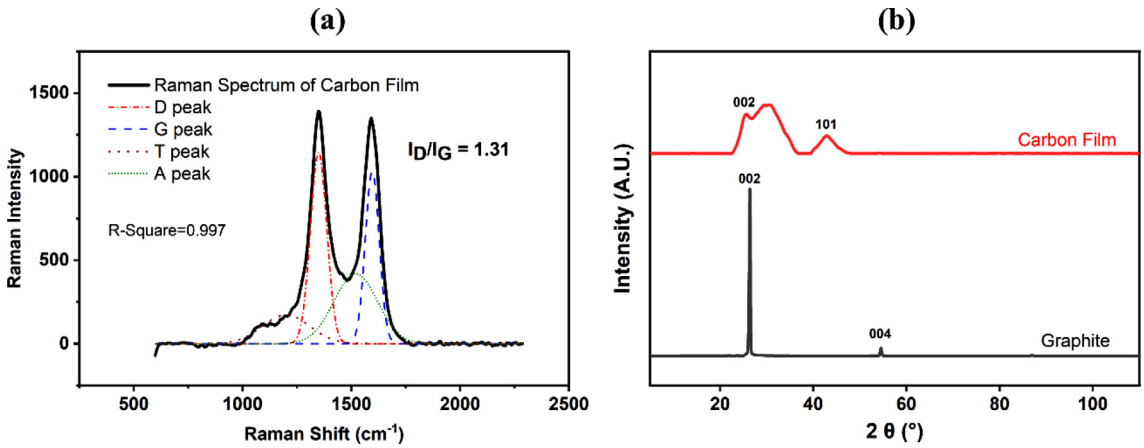


Fig. 4. Raman and X-ray Diffraction (XRD) Spectra of the Carbon Film, Activated Carbon, and Graphite. (a) Deconvoluted Raman spectra of the carbon film, with fitting of D, G, T, and A peaks. (b) XRD spectra of the carbon film compared with graphite suggests the presence of microcrystalline carbon fragments in the carbon film.

further evidence. Specifically, the lateral width of graphite crystals in the carbon film is over three times wider than that in activated carbon, while the increase in stacking height is only slight.

The findings from XRD, XPS, and Raman analysis consistently suggest a semi-graphitic structure of the carbon film. A previous study [59] has reported that heat treatment of carbon films at temperatures exceeding 900 ˚C may transform the structure from an amorphous to a more graphitic one. In this study, the carbon film undergoes heat treatment at 1000 ˚C for approximately two to three hours per experiment; therefore, it is possible to attribute the observed semi-graphitic structure to the heat treatment.

3.4. Cross-sectional and planar characterization of the carbon film using focused ion beam – high-resolution transmission electron microscopy (FIB-HRTEM)

Based on the SEM image presented in Fig. 2c, the carbon film appears to have a thickness of approximately 550 μm. However, to conduct high-resolution transmission electron microscopy (HRTEM), it is desirable to have a sample thickness below 50 nm [60]. Therefore, we focused on the edges of the carbon film, which are often thinner than the center. To examine the carbon film's cross-sectional microstructure, we utilized a focused ion beam (FIB) milling technique. The step-by-step FIB milling process is demonstrated in Fig. 5. Initially, a section of the carbon film, as displayed in Fig. 5a, was chosen. Fig. 5b depicts a secondary electron image of the selected region on the carbon film before the FIB milling procedure, and Fig. 5c shows the carbon film after the process.

The sectioned carbon film was transferred on a TEM sample support chip. The chip was subsequently loaded onto the TEM holder and inserted into the Hitachi HF3300 transmission electron microscope for HRTEM imaging. The second row of Fig. 5 displays a cross-sectional view of the carbon film. High-resolution images unveil the presence of curved carbon nanostructures (Fig. 5d) and a stack of graphitic layers in specific regions (Fig. 5e and 6f) [41]. One possible explanation for the formation of these curved carbon nanostructures is the rolling of graphitic layers during their formation on the inner wall of a cylindrical quartz reactor [61]. Another hypothesis suggests that these curved graphitic layers could be fragments of nearly spherical carbon particles, resulting from the FIB cutting process. However, since the cross-section does not form a complete circle like that of a sphere, this interpretation remains uncertain. Subsequently, these nanosized curved graphitic layers may merge through the deposition of amorphous pyrolytic carbon, align with the observation in the formation of diamond-like carbon films through radio-frequency methane-argon plasma [62]. The shiny dots observed in the first two bright rings of the selected area electron diffraction (SAED) pattern (Fig. 5g) provide additional evidence of the semi-graphitic structure of the carbon film.

In the planar view, we focused on the edges of the carbon film, which are thinner and allow electrons to pass through the specimen, enabling imaging. Despite the selected area electron diffraction (SAED) pattern exhibiting a single bright ring (Fig. 5k), indicating an amorphous structure for the carbon film in the planar direction, Fig. 5i reveals the presence of randomly oriented, curved stacks of carbon layers with thicknesses below 5 nm. These fragments were also found in the TEM analysis of glassy carbon [50], which was characterized as aromatic layer stacks formed at the end of the carbon film formation process [41].

3.5. Mechanism for the formation of thin carbon film

Methane pyrolysis generates light hydrocarbons, including acetylene [63], which serves as a precursor for the formation of heavier hydrocarbons and PAHs (polycyclic aromatic hydrocarbons). Fincke et al. [64] reports that fast cooling of the hot reacting gasses within a few milliseconds hinders the production of PAHs and solid carbon, such as carbon black. Also, Kim et al. [65]. observed the formation of solid carbon when the residence time exceeded 200 ms. In this study, the residence time of the reacting flow at a temperature of approximately 1000°C is around 1.5 second, which is significantly longer than the time required for PAH and solid carbon formation. As a result, there is a possibility that PAHs play a role in driving the formation of the carbon film.

Parker et al. [66] observed the formation of a carbon film through the decomposition of benzene at 1000°C. Their findings suggest that the film formation may primarily be influenced by the presence of polycyclic aromatic hydrocarbons (PAHs) in the gas phase, which can potentially grow and agglomerate to form the carbon film. Therefore, the formation and growth of PAHs in the gas phase could be considered as a potential pathway for carbon film formation.

In our previous study [40], the gas phase species present in the reactor exhaust were analyzed using a gas chromatography-thermal conductivity detector (GC-TCD), and the results indicate that there are only a trivial amount of ethane, ethylene, and acetylene in the exhaust. Acetylene exhibits the lowest concentration among the minor species that exit the reactor, suggesting that it is being consumed through two possible pathways. The first pathway involves the decomposition of acetylene [67] which leads to the formation and growth of polycyclic aromatic hydrocarbons (PAHs), while the second pathway is linked to the addition of acetylene to the carbon surface and PAHs [68]. Additionally, Becker et al. [69] report that benzene and naphthalene both form at nearly the same residence time during methane pyrolysis at temperatures around 1000°C, which is close to the average temperature of our experiments.

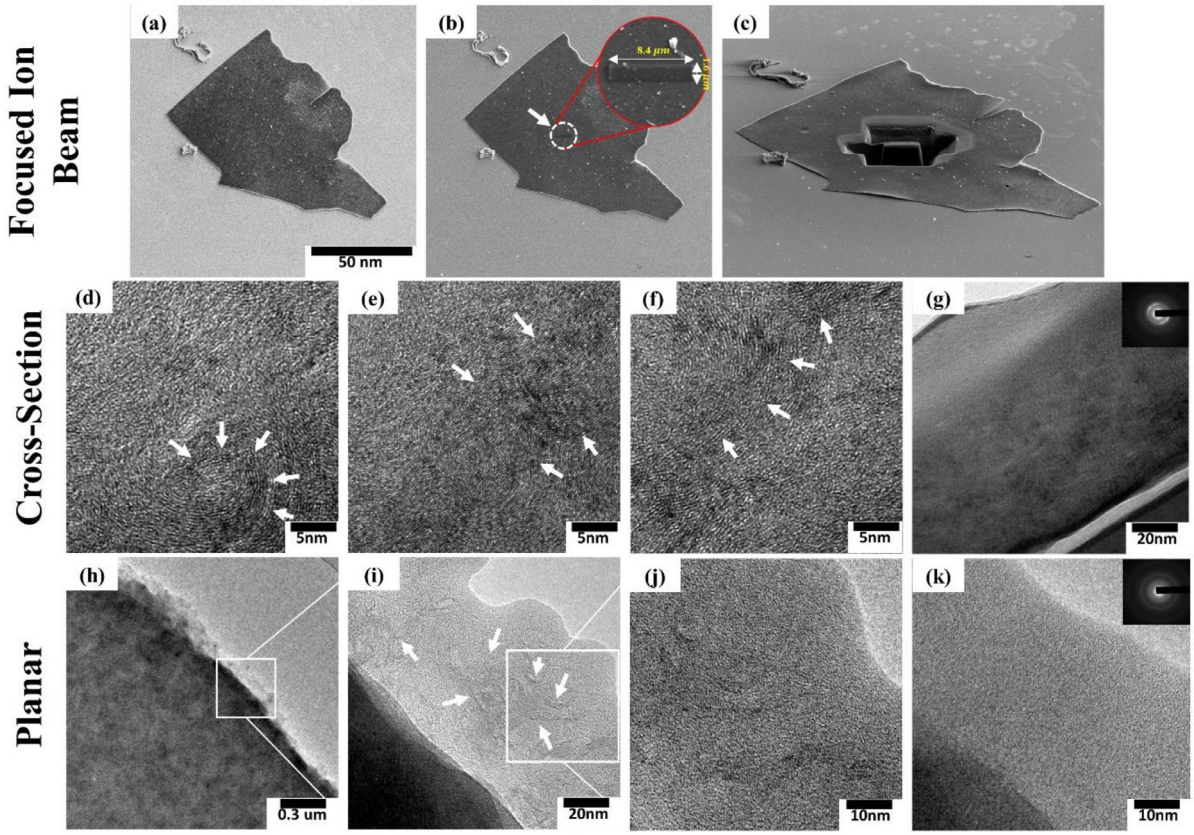


Fig. 5. FIB-HRTEM Characterization of the Carbon Film. The first row illustrates the FIB process steps. The second row displays high-resolution transmission electron microscopy (HRTEM) images of the cross-section of the carbon film, highlighting the existence of curved carbon nanostructures and stack of graphene layers indicated by arrows. The third row depicts the planar view of the carbon film, revealing the presence of fragments from stacks of aromatic layers as indicated by arrows.

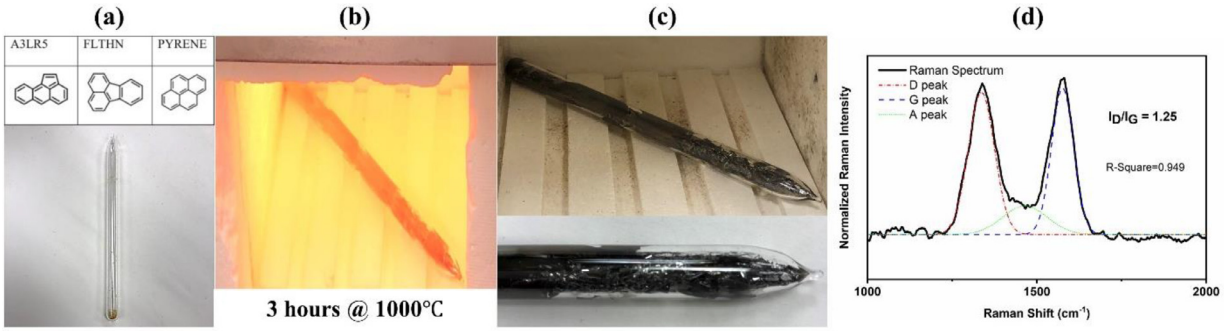


Fig. 6. Formation of Pyrolytic Carbon Film in a Quartz Tube. (a) The quartz vial was filled and sealed with 1 mg each of A3R5, fluoranthene, and pyrene. (b) The vial was placed in a furnace and heat-treated for 3 h at 1000°C. (c) A carbon film was formed on the inner wall of the quartz, and the Raman spectrum of the film suggests a semi-graphitic structure for the carbon film. (d) The Raman spectrum of the produced carbon film.

The previous studies provide evidence suggesting the formation of benzene, which consequently opens the possibility for the formation of pyrene [70,71], Additionally, the reaction between benzene and naphthalene has been observed to yield fluoranthene and acephenanthrylene (A3R5) [70]. The dominance of five-membered ring PAHs may be attributed to the limited number of active sites available on their surface [72,73]. Considering the potential abundance of these PAHs in the gas phase, it would be valuable to explore their potential contribution to the formation of carbon films.

To investigate the role of PAHs in the formation of carbon films, we prepared a mixture of pure PAHs (Sigma Aldrich) containing A3R5, fluoranthene, and pyrene, each at a concentration of 1 mg (Fig. 6a). The mixture was sealed in a quartz vial and heated to 1000°C (Fig. 6b), resulting in the deposition of a carbon film on the tube's inner surface (Fig. 6c). The Raman spectra (Fig. 6d) obtained from the carbon film produced in this experiment were analyzed using the method described in detail in Section 3.3. The analysis suggests a similarity in the D to G peak ratio between the carbon film formed in the quartz vial and the one formed during methane pyrolysis. This similarity suggests a close resemblance in the carbon films' structure and raises the possibility that the formation of this type of carbon film during methane pyrolysis may be independent of the microwave.

3.6. Conductive-Atomic forced microscopy (cAFM) and electrochemical measurements of the carbon film

The conductivity of carbon material is an important factor for its suitability in various applications [74]. Therefore, I-V measurements were

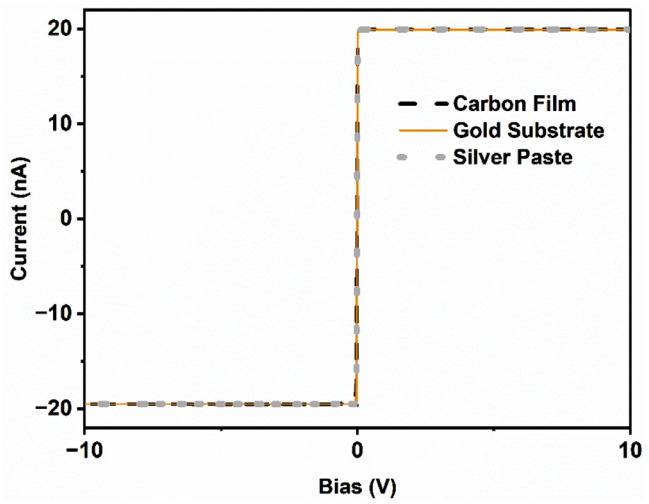


Fig. 7. Comparative cAFM Measurements of the Electrical Conductivity of Carbon Film, Silver, and Gold. The results reveal that carbon film exhibits metallic conductivity, similar to the highly conductive metals (e.g., silver and gold).

conducted on the carbon thin film, silver substrate, and gold substrate using the conductive AFM technique. The ORCA^{TM} module of an Asylum Cypher atomic force microscope (AFM) was utilized for the measurements, which can measure currents ranging from approximately 1 pA to 20 nA. The current flow was measured using conductive AFM probes (12PtIr400B, k = 0.6 N m^{-1}) from Rocky Mountain Nanotechnology. To determine the negligible contact resistance of the system without the carbon thin film, a silver paste was deposited onto a gold substrate and conductivity measurements were conducted. Then, the carbon film was placed onto the gold substrate, and an electrical connection was established to the AFM by using the silver paste. Fig. 7 illustrates the conductivity curve for all three components. The data clearly indicates that the carbon thin film exhibits metallic electrical behavior, similar to that of silver and gold.

The abundant availability of sodium, in contrast to lithium, positions Na-ion batteries as a practical and complementary alternative to the well-established Li-ion batteries [75] that utilize graphite [76]. Therefore, it becomes imperative to find a cost-effective carbon-based material that suits the requirements of Na-ion batteries. The carbon film's high conductivity and free-standing properties make it particularly promising for use in sodium-ion batteries. This is because the film does not require binders or conductive agents, which can enhance the overall performance of the batteries [77]. To evaluate the effectiveness of the carbon film as an active material in sodium-ion batteries, electrochemical measurements were conducted using CR2032 coin cells. For each coin cell, a piece of the carbon film (~8 mm in diameter) was dried overnight in a vacuum oven at 80°C. The coin cells were assembled in an Ar filled glove box with a metallic sodium counter electrode and 1 M NaClO4 in ethylene carbonate (EC) and dimethyl carbonate (DMC) (1:1, v/v) as the electrolyte. The galvanostatic charge/discharge profiles, rate and cycling performance, and the galvanostatic intermittent titration technique (GITT) were performed on LAND CT2001A battery testing system within a potential window of 0–2.5 V.

The first two cycles of the galvanostatic charge/discharge (GCD) curves of the carbon film are shown in Fig. 8a. During this first cycle, the solid electrolyte interphase (SEI) forms on the surface of the electrode and is important for protecting the carbon surface from degradation reactions during cycling. However, the formation of this layer also lowers the Coulombic charging efficiency between the first and second cycle. The carbon film managed to achieve an initial coulombic efficiency (ICE) of 64%, which is reasonable, with the second cycle delivering a capacity of 154 mAh g^{-1}. Examining the rate performance from 0.1C to 2.0C shown in Fig. 8b, the retention of total capacity at 2.0C is 42%. Looking at the discharge curves, it can be seen that the majority of the capacity is largely in the sloping region (>0.1 V), with minimal plateau capacity (Fig. 8d, <0.1 V). It has been proposed that the sloping region

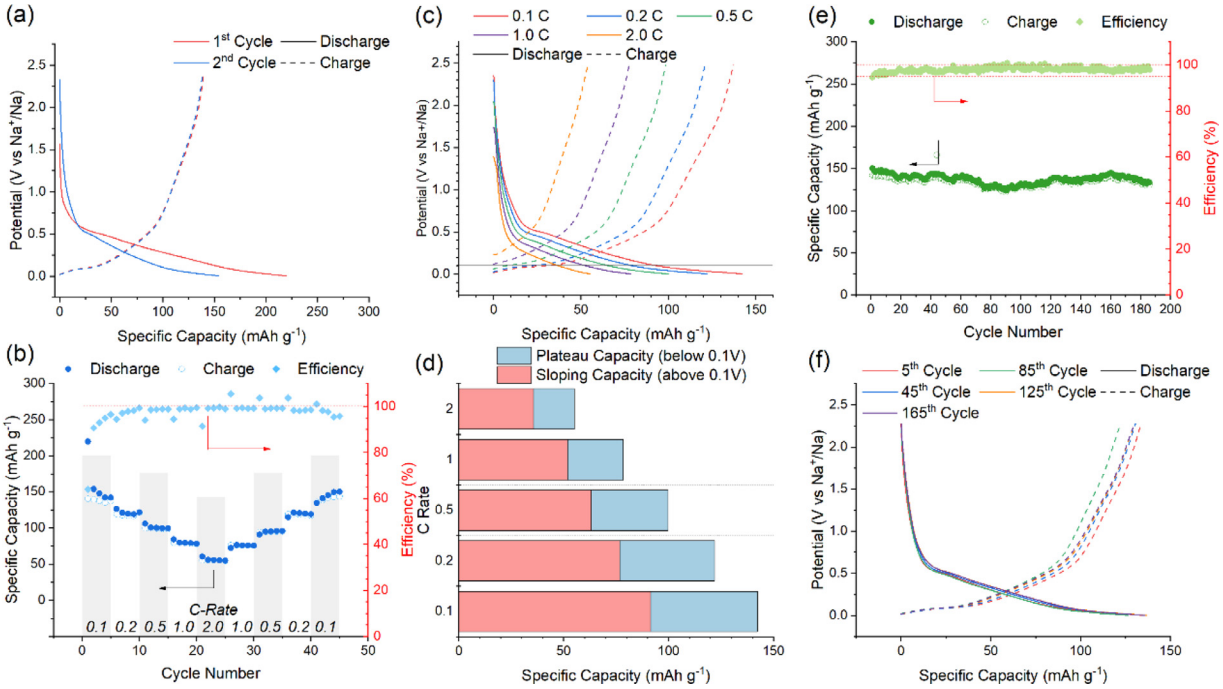


Fig. 8. Electrochemical Measurements of the carbon film. (a) The first and second cycle of the gravimetric charge discharge curves, (b) rate performance at different current densities (C rates), (c) gravimetric charge discharge curves at different current densities, (d) the contributions of sloping at plateau capacities at different current densities, (e) cycling performance at 0.1C, (f) gravimetric charge discharge curves at different cycles.

represents Na+ ions are adsorbed on the defect/edge sites before partial filling of the micropores, whereas in the plateau region Na+ ions are intercalated in the graphitic layers.

To improve the capacity further, the carbon/graphitic structure of the carbon film needs to be modified to allow Na+ intercalation. For the cycling performance at 0.1C (Fig. 8e), the capacity decreased from 150.2 mAh g^{-1} to 134.6 mAh g^{-1} over 180 cycles (89% retention). There was some instability with the cycling, indicating the possible degradation of the carbon or the SEI layer. Overall, the performance of this carbon was lower than the best performing hard carbons in the literature (>280 mAh g^{-1}) [78], however it should be stated that the carbon film was tested as a free-standing electrode without the addition of binders or conductive agents. Thus, the capacities reported are calculated on the full electrode mass, not just the active mass as is reported by some studies in literature. As a free-standing electrode, the performance is promising if the structure can be tuned towards increasing the intercalation of Na+ ions.

4. Conclusions

This study aims to introduce a novel type of carbon film that is synthesized using the microwave-driven methane pyrolysis process. The analysis of the carbon film was conducted using various techniques, including SEM, FIB-HRTEM, XPS, XRD, and c-AFM, to reveal its surface texture, internal structure, composition, and conductivity. SEM imaging results indicate that the carbon film has a smooth surface and a brittle nature. The internal structure of the film was investigated through FIB-HRTEM imaging in both cross-sectional and planar directions. The cross-sectional images revealed a semi-graphitic structure, while the planar images showed mostly amorphous characteristics. Cross-sectional HRTEM images revealed the presence of specific curved stacked graphitic layers connected by amorphous carbon, suggesting that these discrete nanosized graphitic layers may have formed and merged during the pyrolysis process, resulting in a uniform carbon film.

XPS analysis of the film surface reveals that 78% of the carbon atoms are sp2 hybridized, suggesting that the carbon film's surface has a semi-graphitic structure. The analysis also reveals that the film composition is over 97% carbon. Further examination using XRD shows the presence of microcrystalline carbon fragments within the film.

The production of PAHs in the gas phase during the pyrolysis process is found to potentially play a role in the formation of carbon films. To investigate the contribution of PAHs in forming carbon films, a mixture of three PAHs (A3R5, fluoranthene, and pyrene) were sealed in a quartz vial and heated to 1000°C. This resulted in the deposition of a carbon film on the inner surface of the quartz. The similarity between the I_D/I_G ratio of the carbon film formed during the methane pyrolysis process and that of the carbon film on the sealed quartz vial may suggest the significance of PAHs in the formation of the carbon film.

Conductive atomic force microscopy (c-AFM) measurements indicate that the carbon film has high metallic conductivity, comparable to that of gold and silver. Due to the carbon film's semi-graphitic structure and high conductivity, it shows great potential as a conductive agent in batteries. In this study, the carbon film was tested in Na-ion batteries, and the electrochemical measurements suggest that its performance is lower than the best performing hard carbons reported in the literature (>280 mAh g-1), but it can potentially be improved by fine-tuning the production process to modify the structure of the carbon film, as a free-standing electrode, allowing for Na+ intercalation.

CRediT author statement

Mehran Dadsetan: Conceptualization, Methodology, Formal analysis, Investigation, Visualization, Writing - Original Draft, Writing - Review & Editing; **Kenneth G. Latham:** Formal analysis, Investigation, Visualization, Writing - Original Draft; **Boran Kumral:** Formal analysis, Investigation, Visualization, Writing - Original Draft; **Mohammed Fawaz Khan:** Methodology, Formal analysis, Investigation; **Mia Scott:** Investigation, Writing - Original Draft; **Tirthankar Mitra:** Formal analysis, Investigation; **Ali Naseri:** Formal analysis, Investigation; **Sama Manzoor:** Formal analysis, Investigation, Visualization, Writing - Original Draft; **Erin Bobicki:** Formal analysis, Supervision; **Tobin Filleter**: Formal analysis, Writing - Review & Editing, Supervision, **Maria-Magdalena Titirici:** Formal analysis, Writing - Review & Editing, Supervision; **Murray J. Thomson:** Conceptualization, Formal analysis, Writing - Review & Editing, Supervision, Project administration, Funding acquisition.

Declaration of Competing Interest

The authors declare that they have no known competing financial interests or personal relationships that could have appeared to influence the work reported in this paper.

Data availability

Data will be made available on request.

Acknowledgements

This work was supported by the Natural Sciences and Engineering Research Council of Canada (NSERC) [grant RGPIN-2020–06136]. We would like to thank Ontario center for the Characterization of Advanced Materials (OCCAM), Royal Ontario Museum (ROM), and the center for Nanostructure Imaging (CNI) at the University of Toronto for providing the facilities for this research.

References

[1] T.I. Korányi, M. Németh, A. Beck, A. Horváth, Recent Advances in Methane Pyrolysis: turquoise Hydrogen with Solid Carbon Production, Energies (Basel). 15 (2022). doi:10.3390/en15176342.
[2] X. Zeng, D. Fu, H. Sheng, S. Xie, X. Li, Q. Hu, J. Zou, Growth and morphology of carbon nanostructures by microwave-assisted pyrolysis of methane, Physica E Low Dimens. Syst. Nanostruct. 42 (2010) 2103–2108, doi:10.1016/j.physe.2010.04.002.
[3] B. Fidalgo, Y. Fernández, A. Domínguez, J.J. Pis, J.A. Menéndez, Microwave-assisted pyrolysis of CH4/N2 mixtures over activated carbon, J. Anal. Appl. Pyrolysis 82 (2008) 158–162, doi:10.1016/j.jaap.2008.03.004.
[4] Z.J. Hu, W.G. Zhang, K.J. Hüttinger, B. Reznik, D. Gerthsen, Influence of pressure, temperature and surface area/volume ratio on the texture of pyrolytic carbon deposited from methane, Carbon N Y 41 (2003) 749–758, doi:10.1016/S0008-6223(02)00403-7.
[5] E. Sun, S. Zhai, D. Kim, M. Gigantino, V. Haribal, O.S. Dewey, S.M. Williams, G. Wan, A. Nelson, S. Marin-Quiros, J. Martis, C. Zhou, J. Oh, R. Randall, M. Kessler, D. Kong, J. Rojas, A. Tong, X. Xu, C. Huff, M. Pasquali, R. Gupta, M. Cargnello, A. Majumdar, A semi-continuous process for co-production of CO2-free hydrogen and carbon nanotubes via methane pyrolysis, Cell Rep. Phys. Sci. (2023) 101338, doi:10.1016/j.xcrp.2023.101338.
[6] M. Gautier, V. Rohani, L. Fulcheri, Direct decarbonization of methane by thermal plasma for the production of hydrogen and high value-added carbon black, Int. J. Hydrogen Energy 42 (2017) 28140–28156, doi:10.1016/j.ijhydene.2017.09.021.
[7] N. Uhlenbruck, B. Dietrich, C. Hofberger, L. Stoppel, T. Wetzel, Methane Pyrolysis in a Liquid Metal Bubble Column Reactor: a Model Approach Combining Bubble Dynamics with Byproduct and Soot Formation, Energy Technol. 10 (2022) 2200654, doi:10.1002/ente.202200654.
[8] P. Lucas, A. Marchand, Pyrolytic carbon deposition from methane: an analytical approach to the chemical process, Carbon N Y 28 (1990) 207–219, doi:10.1016/0008-6223(90)90115-F.
[9] S. Aisenberg, R. Chabot, Ion-Beam Deposition of Thin Films of Diamondlike Carbon, J. Appl. Phys. 42 (1971) 2953–2958, doi:10.1063/1.1660654.
[10] P. Mérel, M. Tabbal, M. Chaker, S. Moisa, J. Margot, Direct evaluation of the sp3 content in diamond-like-carbon films by XPS, Appl. Surf. Sci. 136 (1998) 105–110, doi:10.1016/S0169-4332(98)00319-5.
[11] A. Grill, Diamond-like carbon: state of the art, Diam. Relat. Mater. 8 (1999) 428–434, doi:10.1016/S0925-9635(98)00262-3.
[12] K.E. Spear, J.P. Dismukes, Synthetic diamond: Emerging CVD Science and Technology, John Wiley & Sons, 1994.
[13] T.V. Choudhary, E. Aksoylu, D. Wayne Goodman, Nonoxidative Activation of Methane, Catal. Rev. 45 (2003) 151–203, doi:10.1081/CR-120017010.
[14] W. Ren, H.-M. Cheng, The global growth of graphene, Nat. Nanotechnol. 9 (2014) 726–730, doi:10.1038/nnano.2014.229.
[15] Y. Hernandez, V. Nicolosi, M. Lotya, F.M. Blighe, Z. Sun, S. De, I.T. McGovern, B. Holland, M. Byrne, Y.K. Gun'Ko, J.J. Boland, P. Niraj, G. Duesberg, S. Krishnamurthy,

R. Goodhue, J. Hutchison, V. Scardaci, A.C. Ferrari, J.N. Coleman, High-yield production of graphene by liquid-phase exfoliation of graphite, Nat. Nanotechnol. 3 (2008) 563–568, doi:10.1038/nnano.2008.215.
[16] D. Parviz, F. Irin, S.A. Shah, S. Das, C.B. Sweeney, M.J. Green, Challenges in Liquid-Phase Exfoliation, Processing, and Assembly of Pristine Graphene, Adv. Mater. 28 (2016) 8796–8818, doi:10.1002/adma.201601889.
[17] F. Wang, F. Wang, R. Hong, X. Lv, Y. Zheng, H. Chen, High-purity few-layer graphene from plasma pyrolysis of methane as conductive additive for LiFePO4 lithium ion battery, J. Mater. Res. Technol. 9 (2020) 10004–10015, doi:10.1016/j.jmrt.2020.06.072.
[18] M. Rasheed, S. Shihab, O.W. Sabah, An investigation of the structural, electrical and optical properties of graphene-oxide thin films using different solvents, J. Phys. Conf. Ser. (2021) 012052.
[19] E.P. Neustroev, A.R. Prokopyev, S.O. Semenov, V.I. Popov, F.F. Protopopov, A.S. Andreev, N.A. Savvinova, E.S. Lukin, Research of Properties of a Carbon Film Formed in Methane Plasma and the Following Annealing, IOP Conf. Ser. Mater. Sci. Eng. 1079 (2021) 042086, doi:10.1088/1757-899X/1079/4/042086.
[20] G. Eda, M. Chhowalla, Chemically Derived Graphene Oxide: towards Large-Area Thin-Film Electronics and Optoelectronics, Adv. Mater. 22 (2010) 2392–2415, doi:10.1002/adma.200903689.
[21] O. Jašek, J. Toman, M. Šnírer, J. Jurmanová, V. Kudrle, J. Michalička, D. Všianský, D. Pavliňák, Microwave plasma-based high temperature dehydrogenation of hydrocarbons and alcohols as a single route to highly efficient gas phase synthesis of freestanding graphene, Nanotechnology 32 (2021) 505608, doi:10.1088/1361-6528/ac24c3.
[22] O. Jašek, J. Toman, D. Všianský, J. Jurmanová, M. Šnírer, D. Hemzal, A.G. Bannov, J. Hajzler, P. St'ahel, V. Kudrle, Controlled high temperature stability of microwave plasma synthesized graphene nanosheets, J. Phys. D Appl. Phys. 54 (2021) 165201, doi:10.1088/1361-6463/abdb6d.
[23] N. Bundaleska, D. Tsyganov, A. Dias, E. Felizardo, J. Henriques, F.M. Dias, M. Abrashev, J. Kissovski, E. Tatarova, Microwave plasma enabled synthesis of free standing carbon nanostructures at atmospheric pressure conditions, Phys. Chem. Chem. Phys. 20 (2018) 13810–13824, doi:10.1039/C8CP01896K.
[24] M. Singh, A. Sengupta, K. Zeller, G. Skoptsov, R.L. Vander Wal, Effect of hydrogen concentration on graphene synthesis using microwave-driven plasma-mediated methane cracking, Carbon N Y 143 (2019) 802–813, doi:10.1016/j.carbon.2018.11.082.
[25] P. Fortugno, S. Musikhin, X. Shi, H. Wang, H. Wiggers, C. Schulz, Synthesis of free-standing few-layer graphene in microwave plasma: the role of oxygen, Carbon N Y 186 (2022) 560–573, doi:10.1016/j.carbon.2021.10.047.
[26] C. Wang, D. Li, Z. Lu, M. Song, W. Xia, Synthesis of carbon nanoparticles in a non-thermal plasma process, Chem. Eng. Sci. 227 (2020) 115921, doi:10.1016/j.ces.2020.115921.
[27] Y. Ando, X. Zhao, M. Ohkohchi, Production of petal-like graphite sheets by hydrogen arc discharge, Carbon N Y 35 (1997) 153–158, doi:10.1016/S0008-6223(96)00139-X.
[28] A. Dato, V. Radmilovic, Z. Lee, J. Phillips, M. Frenklach, Substrate-Free Gas-Phase Synthesis of Graphene Sheets, Nano Lett. 8 (2008) 2012–2016, doi:10.1021/nl8011566.
[29] Y. Sun, Z. Chen, H. Gong, X. Li, Z. Gao, S. Xu, X. Han, B. Han, X. Meng, J. Zhang, Continuous "Snowing" Thermotherapeutic Graphene, Adv. Mater. 32 (2020) 2002024, doi:10.1002/adma.202002024.
[30] Y. Sun, L. Yang, K. Xia, H. Liu, D. Han, Y. Zhang, J. Zhang, Snowing" Graphene using Microwave Ovens, Adv. Mater. 30 (2018) 1803189, doi:10.1002/adma.201803189.
[31] H. Zhang, T. Cao, Y. Cheng, Preparation of few-layer graphene nanosheets by radio-frequency induction thermal plasma, Carbon N Y 86 (2015) 38–45, doi:10.1016/j.carbon.2015.01.021.
[32] X. Li, B. Bhushan, Micro/nanomechanical and tribological characterization of ultrathin amorphous carbon coatings, J. Mater. Res. 14 (1999) 2328–2337, doi:10.1557/JMR.1999.0309.
[33] G.M. Pharr, D.L. Callahan, S.D. McAdams, T.Y. Tsui, S. Anders, A. Anders, J.W. Ager III, I.G. Brown, C.S. Bhatia, S.R.P. Silva, J. Robertson, Hardness, elastic modulus, and structure of very hard carbon films produced by cathodic-arc deposition with substrate pulse biasing, Appl. Phys. Lett. 68 (1996) 779–781, doi:10.1063/1.116530.
[34] R. Paul, S.N. Das, S. Dalui, R.N. Gayen, R.K. Roy, R. Bhar, A.K. Pal, Synthesis of DLC films with different sp2/sp3 ratios and their hydrophobic behaviour, J. Phys. D Appl. Phys. 41 (2008) 055309, doi:10.1088/0022-3727/41/5/055309.
[35] Y. Gao, T. Cao, F. Cellini, C. Berger, W.A. de Heer, E. Tosatti, E. Riedo, A. Bongiorno, Ultrahard carbon film from epitaxial two-layer graphene, Nat. Nanotechnol. 13 (2018) 133–138, doi:10.1038/s41565-017-0023-9.
[36] John Robertson, Electronic and atomic structure of diamond-like carbon, Semicond. Sci. Technol. 18 (2003) S12, doi:10.1088/0268-1242/18/3/302.
[37] A.M.M. Omer, S. Adhikari, S. Adhikary, M. Rusop, H. Uchida, T. Soga, M. Umeno, Electrical conductivity improvement by iodine doping for diamond-like carbon thin-films deposited by microwave surface wave plasma CVD, Diam. Relat. Mater. 15 (2006) 645–648, doi:10.1016/j.diamond.2005.11.045.
[38] S.U. Singh, S. Chatterjee, S.A. Lone, H.-H. Ho, K. Kaswan, K. Peringeth, A. Khan, Y.-W. Chiang, S. Lee, Z.-H. Lin, Advanced wearable biosensors for the detection of body fluids and exhaled breath by graphene, Microchimica Acta 189 (2022) 236, doi:10.1007/s00604-022-05317-2.
[39] Q. Xiang, J. Yu, M. Jaroniec, Graphene-based semiconductor photocatalysts, Chem. Soc. Rev. 41 (2012) 782–796.
[40] M. Dadsetan, M.F. Khan, M. Salakhi, E.R. Bobicki, M.J. Thomson, CO2-free hydrogen production via microwave-driven methane pyrolysis, Int. J. Hydrogen Energy (2023), doi:10.1016/j.ijhydene.2022.12.353.
[41] J.-F. Després, C. Vahlas, A. Oberlin, Chemical vapor deposition of pyrolytic carbon on polished substrates, Le Journal de Physique IV 3 (1993) C3–563.
[42] G. Paredes, T. Ondarçuhu, M. Monthioux, F. Piazza, Unveiling the existence and role of a liquid phase in a high temperature (1400°C) pyrolytic carbon deposition process, Carbon Trends 5 (2021) 100117, doi:10.1016/j.cartre.2021.100117.
[43] J. Lefebvre, F. Galli, C.L. Bianchi, G.S. Patience, D.C. Boffito, Experimental methods in chemical engineering: x-ray photoelectron spectroscopy-XPS, Can. J. Chem. Eng. 97 (2019) 2588–2593, doi:10.1002/cjce.23530.
[44] X. Chen, X. Wang, D. Fang, A review on C1s XPS-spectra for some kinds of carbon materials, Fullerenes, Nanotubes Carbon Nanostruct. 28 (2020) 1048–1058.
[45] L.R. Radovic, A.B. Silva-Tapia, F. Vallejos-Burgos, Oxygen migration on the graphene surface. 1. Origin of epoxide groups, Carbon N Y 49 (2011) 4218–4225, doi:10.1016/j.carbon.2011.05.059.
[46] D. Pantea, H. Darmstadt, S. Kaliaguine, L. Sümmchen, C. Roy, Electrical conductivity of thermal carbon blacks: influence of surface chemistry, Carbon N Y 39 (2001) 1147–1158, doi:10.1016/S0008-6223(00)00239-6.
[47] A. Wollbrink, C.H. Rüscher, K. Volgmann, J. Koch, A. Breuksch, C. Tegenkamp, J. Caro, Improved hydrogen selectivity of Surface Modified Graphite (SMG) membranes: permeation experiments and characterisation by micro-Raman spectroscopy and XPS, J. Memb. Sci. 528 (2017) 316–325, doi:10.1016/j.memsci.2016.12.067.
[48] A. Ganguly, S. Sharma, P. Papakonstantinou, J. Hamilton, Probing the Thermal Deoxygenation of Graphene Oxide Using High-Resolution In Situ X-ray-Based Spectroscopies, J. Phys. Chem. C 115 (2011) 17009–17019, doi:10.1021/jp203741y.
[49] R. Al-Gaashani, A. Najjar, Y. Zakaria, S. Mansour, M.A. Atieh, XPS and structural studies of high quality graphene oxide and reduced graphene oxide prepared by different chemical oxidation methods, Ceram. Int. 45 (2019) 14439–14448, doi:10.1016/j.ceramint.2019.04.165.
[50] H. Diaf, A. Pereira, P. Melinon, N. Blanchard, F. Bourquard, F. Garrelie, C. Donnet, M. Vondráček, Revisiting thin film of glassy carbon, Phys. Rev. Mater. 4 (2020) 66002, doi:10.1103/PhysRevMaterials.4.066002.
[51] F. Tuinstra, J.L. Koenig, Raman Spectrum of Graphite, J. Chem. Phys. 53 (1970) 1126–1130, doi:10.1063/1.1674108.
[52] Y. Wang, D.C. Alsmeyer, R.L. McCreery, Raman spectroscopy of carbon materials: structural basis of observed spectra, Chem. Mater. 2 (1990) 557–563, doi:10.1021/cm00011a018.
[53] A. Sadezky, H. Muckenhuber, H. Grothe, R. Niessner, U. Pöschl, Raman microspectroscopy of soot and related carbonaceous materials: spectral analysis and structural information, Carbon N Y 43 (2005) 1731–1742, doi:10.1016/j.carbon.2005.02.018.
[54] L.G. Cançado, M.A. Pimenta, B.R.A. Neves, M.S.S. Dantas, A. Jorio, Influence of the Atomic Structure on the Raman Spectra of Graphite Edges, Phys. Rev. Lett. 93 (2004) 247401, doi:10.1103/PhysRevLett.93.247401.
[55] S. Zhang, Q. Liu, H. Zhang, R. Ma, K. Li, Y. Wu, B.J. Teppen, Structural order evaluation and structural evolution of coal derived natural graphite during graphitization, Carbon N Y 157 (2020) 714–723, doi:10.1016/j.carbon.2019.10.104.
[56] J. Biscoe, B.E. Warren, An x-ray study of carbon black, J. Appl. Phys. 13 (1942) 364–371, doi:10.1063/1.1714879.
[57] M. Waseem, S. Mustafa, A. Naeem, K. Shah, Synthesis and characterization of silica by sol-gel method Adsorption of pollutants onto nano-sorbents View project Preparation, characterization and applications of some functional materials View project, 2009. https://www.researchgate.net/publication/285105909.
[58] Y. Tang, Q. Liu, F. Chen, Preparation and characterization of activated carbon from waste ramulus mori, Chem. Eng. J. 203 (2012) 19–24, doi:10.1016/j.cej.2012.07.007.
[59] G.K. Kiema, M.J. Brett, Effect of thermal annealing on structural properties and electrochemical performance of carbon films with porous microstructure, J. Electrochem. Soc. 151 (2004) E194.
[60] D.B. Williams, C.B. Carter, The Transmission Electron Microscope BT - Transmission Electron Microscopy: A Textbook For Materials Science, in: D.B. Williams, C.B. Carter (Eds.), Springer US, Boston, MA, 1996: pp. 3–17. doi:10.1007/978-1-4757-2519-3_1.
[61] X.H. Chen, H.S. Yang, G.T. Wu, M. Wang, F.M. Deng, X.B. Zhang, J.C. Peng, W.Z. Li, Generation of curved or closed-shell carbon nanostructures by ball-milling of graphite, J. Cryst. Growth 218 (2000) 57–61, doi:10.1016/S0022-0248(00)00486-3.
[62] R. Maheswaran, S. Ramaswamy, D.J. Thiruvadigal, C. Gopalakrishnan, Systematic study of various stages during the growth process of diamond-like carbon film by atomic force microscopy, J. Non Cryst. Solids 357 (2011) 1710–1715, doi:10.1016/j.jnoncrysol.2011.02.012.
[63] H. An, Y. Cheng, T. Li, Y. Li, Y. Cheng, Numerical analysis of methane pyrolysis in thermal plasma for selective synthesis of acetylene, Fuel Process. Technol. 172 (2018) 195–199, doi:10.1016/j.fuproc.2017.12.025.
[64] J.R. Fincke, R.P. Anderson, T. Hyde, B.A. Detering, R. Wright, R.L. Bewley, D.C. Haggard, W.D. Swank, Plasma thermal conversion of methane to acetylene, Plasma Chem. Plasma Process. 22 (2002) 105–136, doi:10.1023/A:1012944615974.
[65] K.S. Kim, J.H. Seo, J.S. Nam, W.T. Ju, S.H. Hong, Production of hydrogen and carbon black by methane decomposition using DC-RF hybrid thermal plasmas, IEEE Trans. Plasma Sci. 33 (2005) 813–823, doi:10.1109/TPS.2005.844526.
[66] J.F. Parker, C.R. So, M.B. Sassin, J.S. Ko, S. Jeon, C.N. Chervin, J.C. Lytle, M.E. Helms, D.R. Rolison, J.W. Long, Pyrolytic Carbon Films with Tunable Electronic Structure and Surface Functionality: a Planar Stand-In for Electroanalysis of Energy-Relevant Reactions, ChemElectroChem 7 (2020) 672–683, doi:10.1002/celc.201901672.
[67] N.E. Sánchez, Á. Millera, R. Bilbao, M.U. Alzueta, Polycyclic aromatic hydrocarbons (PAH), soot and light gases formed in the pyrolysis of acetylene at different temperatures: effect of fuel concentration, J. Anal. Appl. Pyrolysis 103 (2013) 126–133, doi:10.1016/j.jaap.2012.10.027.

[68] M. Frenklach, H. Wang, Detailed modeling of soot particle nucleation and growth, Symp. (Int.) Combust. 23 (1991) 1559–1566, doi:10.1016/S0082-0784(06)80426-1.
[69] A. Becker, K.J. Hüttinger, Chemistry and kinetics of chemical vapor deposition of pyrocarbon — IV pyrocarbon deposition from methane in the low temperature regime, Carbon N Y 36 (1998) 213–224, doi:10.1016/S0008-6223(97)00177-2.
[70] G.L. Dong, K.J. Hüttinger, Consideration of reaction mechanisms leading to pyrolytic carbon of different textures, Carbon N Y 40 (2002) 2515–2528, doi:10.1016/S0008-6223(02)00174-4.
[71] P. Lott, M.B. Mokashi, H. Müller, D.J. Heitlinger, S. Lichtenberg, A.B. Shirsath, C. Janzer, S. Tischer, L. Maier, O. Deutschmann, Hydrogen Production and Carbon Capture by Gas-Phase Methane Pyrolysis: a Feasibility Study, ChemSusChem (2022) e202201720 n/a, doi:10.1002/cssc.202201720.
[72] Z. Li, Experimental and theoretical study of PAH and incipient soot formation in laminar flames, 2021. http://hdl.handle.net/10754/668805.
[73] L. Zhao, Ralf.I. Kaiser, W. Lu, B. Xu, M. Ahmed, A.N. Morozov, A.M. Mebel, A.H. Howlader, S.F. Wnuk, Molecular mass growth through ring expansion in polycyclic aromatic hydrocarbons via radical–radical reactions, Nat. Commun. 10 (2019) 3689, doi:10.1038/s41467-019-11652-5.
[74] X. Zhang, Y. Cui, Z. Lv, M. Li, S. Ma, Z. Cui, Q. Kong, Carbon nanotubes, conductive carbon black and graphite powder based paste electrodes, Int. J. Electrochem. Sci. 6 (2011) 6063–6073.
[75] J. Deng, W.B. Luo, S.L. Chou, H.K. Liu, S.X. Dou, Sodium-Ion Batteries: from Academic Research to Practical Commercialization, Adv. Energy Mater. 8 (2018) 1701428, doi:10.1002/aenm.201701428.
[76] K. Ozawa, Lithium-ion rechargeable batteries with LiCoO2 and carbon electrodes: the LiCoO2/C system, Solid State Ion 69 (1994) 212–221, doi:10.1016/0167-2738(94)90411-1.
[77] T. Jin, Q. Han, L. Jiao, Binder-free electrodes for advanced sodium-ion batteries, Adv. Mater. 32 (2020) 1806304, doi:10.1002/adma.201806304.
[78] J. Conder, C. Villevieille, J.-M.L. Meins, C.M. Ghimbeu, Is there a ready recipe for hard carbon electrode engineering to enhance Na-ion battery performance? ACS Appl. Energy Mater. 5 (2022) 12373–12387, doi:10.1021/acsaem.2c01984.